Wrinkled axicons: shaping light from cusps.

Benjamin Sanchez-Padilla, Albertas Žukauskas, Artur Aleksanyan, Armandas Balčytis, Mangirdas Malinauskas, Saulius Juodkazis, Etienne Brasselet

Wrinkled axicons: shaping light from cusps

Benjamin Sanchez-Padilla,[1,2] Albertas Žukauskas,[3] Artur Aleksanyan,[1,2] Armandas Balčytis,[4] Mangirdas Malinauskas,[3] Saulius Juodkazis,[4] and Etienne Brasselet[1,2,*]

[1] *Univ. Bordeaux, LOMA, UMR 5798, F-33400 Talence, France*
[2] *CNRS, LOMA, UMR 5798, F-33400 Talence, France*
[3] *Department of Quantum Electronics, Physics Faculty, Vilnius University, Sauletekio Ave. 10, LT-10223 Vilnius, Lithuania*
[4] *Centre for Micro-Photonics, Faculty of Engineering and Industrial Sciences, Swinburne University of Technology, Hawthorn, VIC 3122, Australia*
[*] *etienne.brasselet@u-bordeaux.fr*

Abstract: We propose a novel class of refractive optical elements by wrinkling the conical surface of a usual (conical) axicon, which leads to geometrical singularities (cusps). Such wrinkled axicons have been fabricated at the micron scale by using three-dimensional femtosecond-laser photopolymerization technique and we report on their experimental and numerical characterization. The beam shaping capabilities of these structures are discussed for both intensity and phase, which includes topological beam shaping that results from azimuthally modulated optical spin-orbit interaction.

OCIS codes: (350.3950) Micro-optics; (140.3390) Laser materials processing; (260.6042) Singular optics.

References and links

1. S. N. Khonina, V. V. Kotlyar, M. V. Shinkaryev, V. A. Soifer, and G. V. Uspleniev, "The phase rotor filter," J. Mod. Opt. **39**, 1147–1154 (1992).
2. J. H. McLeod, "The axicon: a new type of optical element," J. Opt. Soc. Am. **44**, 592–592 (1954).
3. O. Ren and R. Birngruber, "Axicon: a new laser beam delivery system for corneal surgery," IEEE J. Quantum Electron. **26**, 2305–2308 (1990).
4. D. McGloin and K. Dholakia, "Bessel beams: diffraction in a new light," Contemp. Phys. **46**, 15–28 (2005).
5. M. Duocastella and C. B. Arnold, "Bessel and annular beams for materials processing," Laser Photon. Rev. **6**, 607–621 (2012).
6. A. Vasara, J. Turunen, and A. T. Friberg, "Realization of general nondiffracting beams with computer-generated holograms," J. Opt. Soc. Am. A **6**, 1748–1754 (1989).
7. J. Arlt and K. Dholakia, "Generation of high-order bessel beams by use of an axicon," Opt. Commun. **177**, 297–301 (2000).
8. E. Brasselet, "Optical vortices from closed-loop subwavelength slits," Opt. Lett. **103**, 2575–2577 (2013).
9. E. Brasselet, G. Gervinskas, G. Seniutinas, and S. Juodkazis, "Topological shaping of light by closed-path nanoslits," Phys. Rev. Lett. **103**, 193901 (2013).
10. M. Malinauskas, A. Zukauskas, S. Hasegawa, Y. Hayasaki, V. Mizeikis, R. Buividas, and S. Juodkazis, "Ultrafast laser processing of materials: from science to industry," Light Sci. Appl. **5**, e16133 (2016).
11. A. Ovsianikov, J. Viertl, B. Chichkov, M. Oubaha, B. MacCraith, I. Sakellari, A. Giakoumaki, D. Gray, M. Vamvakaki, M. Farsari, and C. Fotakis, "Ultra-low shrinkage hybrid photosensitive material for two-photon polymerization microfabrication," ACS Nano **2**, 2257–2262 (2008).
12. J. Arlt and M. J. Padgett, "Generation of a beam with a dark focus surrounded by regions of higher intensity: the optical bottle beam," Opt. Lett. **25**, 191–193 (2000).
13. S. Chavez-Cerda, E. Tepichin, M. A. Meneses-Nava, G. Ramirez, and J. M. Hickmann, "Experimental observation of interfering bessel beams," Opt. Express **3**, 524–529 (1998).
14. D. McGloin, G. Spalding, H. Melville, W. Sibbett, and K. Dholakia, "Three-dimensional arrays of optical bottle beams," Opt. Commun. **225**, 215–222 (2003).
15. A. Aleksanyan and E. Brasselet, "Spin-orbit photonic interaction engineering of bessel beams," Optica **3**, 167–174 (2016).
16. K. Y. Bliokh, E. A. Ostrovskaya, M. A. Alonso, O. G. Rodríguez-Herrera, D. Lara, and C. Dainty, "Spin-to-orbital angular momentum conversion in focusing, scattering, and imaging systems," Opt. Express **19**, 26132–26149 (2011).

17. K. Y. Bliokh, M. A. Alonso, E. A. Ostrovskaya, and A. Aiello, "Angular momenta and spin-orbit interaction of nonparaxial light in free space," Phys. Rev. A **82**, 063825 (2010).
18. P. J. Lavery, D. J. Robertson, G. C. G. Berkhout, G. D. Love, M. J. Padgett, and J. Courtial, "Refractive elements for the measurement of the orbital angular momentum of a single photon," Opt. Express **20**, 2110–2115 (2012).
19. M. Mirhosseini, M. Malik, Z. Shi, and R. W. Boyd, "Efficient separation of the orbital angular momentum eigenstates of light," Nat. Commun. **4**, 2781 (2012).
20. G. Knöner, S. Parkin, T. A. Nieminen, V. L. Y. Loke, N. R. Heckenberg, and H. Rubinsztein-Dunlop, "Integrated optomechanical microelements," Opt. Express **15**, 5521–5530 (2007).
21. E. Brasselet, M. Malinauskas, A. Žukauskas, and S. Juodkazis, "Photo-polymerized microscopic vortex beams generators: precise delivery of optical orbital angular momentum," Appl. Phys. Lett. **97**, 211108 (2010).
22. A. Žukauskas, M. Malinauskas, and E. Brasselet, "Monolithic generators of pseudo-nondiffracting optical vortex beams at the microscale," Appl. Phys. Lett. **103**, 181122 (2013).

1. Introduction

Lenses are refractive optical elements to focus light and form images. They generally consist of a polished piece of transparent material whose shape defines its use. Spherical lenses correspond to the most popular design where the lens shape is defined by two spherical surfaces. More complex shapes are also common, such as astigmatic lenses whose shape is defined by at least one surface having two distinct radii of curvature. Aspheric lenses are another example where at least one surface has neither spherical nor cylindrical design, which finds use to minimize spherical aberrations. All these cases refer to smooth surface geometries, however some situations imply the use of singular designs such as helical or conical surfaces. The former example refers to refractive spiral phase plates introduced in 1992 [1] that are nowadays widely used to generate optical vortex beams associated with helical wavefronts. The latter case refers to conical lenses, which belong to the family of axicons introduced in 1954 in the context of optical imaging [2].

Unlike usual lenses, axicons are characterized by a long depth of focus defined as $\zeta_0 = w_0/[(n-1)\alpha_0]$ where w_0 is the radius of the beam entering the axicon, n is the refractive index of the axicon, and $\alpha_0 = \arctan(H/R)$ (assumed to be small in the above expression) with H the height of the cone and R the radius of the flat base. Besides imaging applications associated with extended focus region, their practical use also encompasses beam shaping into a ring or the generation of close approximation of non-diffractive Bessel beams, which find many applications such as laser eye surgery [3], optical trapping and optical manipulation [4], or processing of materials [5].

Bessel beams form a family of non-diffractive fields, each element being associated with mth-order Bessel function within the paraxial approximation [4]. In practice, higher-order Bessel beams ($m \geq 0$) can be obtained from Gaussian beams by using binary amplitude masks [6] or from Laguerre-Gaussian beams passing through usual axicons [7]. Here we propose a novel class of higher-order axicons obtained by wrinkling the conical surface of a usual axicon. This is made by introducing cusp deformations of the circular shape of a conical lens, namely hypocycloidal (H) and epicycloidal (E) geometries for the purpose of demonstration. As such, this work can be viewed as the birefringence-free three-dimensional (3D) extension of a previous study dedicated to the topological shaping of light from form-birefringent cuspy metallic nanoslits [8, 9].

2. Design and fabrication

Wrinkled axicons are fabricated at the micron scale by using 3D femtosecond-laser photopolymerization technique [10], the fabrication parameters being given below. This is illustrated in Fig. 1 that displays scanning electron microscope images of H- and E-axicons of various order m that refers to the number of cusps of any cross-section of the optical element in a plane perpendicular to the axicon axis. The corresponding designs are obtained by constructing cones with base (located at $z = 0$) having hypocycloidal or epicycloidal shapes. On the one hand,

H-axicons of order $m \geq 3$ are defined by their surface

$$x_{\mathrm{H}m}(\rho,\theta) = \frac{\rho R}{m}\Big\{(m-1)\cos\theta + \cos[(m-1)\theta]\Big\}, \quad (1)$$

$$y_{\mathrm{H}m}(\rho,\theta) = \frac{\rho R}{m}\Big\{(m-1)\sin\theta - \sin[(m-1)\theta]\Big\}, \quad (2)$$

$$z_{\mathrm{H}m}(\rho) = (1-\rho)H, \quad (3)$$

with $0 \leq \theta \leq 2\pi$ and $0 \leq \rho \leq 1$. On the other hand, E-axicons of order $m \geq 1$ are defined by

$$x_{\mathrm{E}m}(\rho,\theta) = \frac{\rho R}{m+2}\Big\{(m+1)\cos\theta - \cos[(m+1)\theta]\Big\}, \quad (4)$$

$$y_{\mathrm{E}m}(\rho,\theta) = \frac{\rho R}{m+2}\Big\{(m+1)\sin\theta - \sin[(m+1)\theta]\Big\}, \quad (5)$$

$$z_{\mathrm{E}m}(\rho) = (1-\rho)H, \quad (6)$$

also with $0 \leq \theta \leq 2\pi$ and $0 \leq \rho \leq 1$. Note that the parametrization variable θ should not be confused with the usual azimuthal angle ϕ the (x, y) plane that satisfies $\tan\phi = y/x$.

In practice, various microscopic wrinkled axicons with fixed $R = 50$ μm are prepared using already well established direct laser writing 3D lithography technique [10] using the SZ2080 material [11] doped with 2 wt% 2-benzyl-2-(dimethylamino)-4'-morpholinobutyrophenone (from Sigma Aldrich) acting as a photoinitiator. The employed setup consisted of femtosecond light source (Pharos, from Light Conversion) with 300 fs pulse width, 515 nm central wavelength, 200 kHz repetition rate and 35 μW optical power. Sample translation stages are synchronized with galvanometric-scanner for beam deflection (assembled by Altechna R&D). The beam is focused via microscope objective with magnification 63× and numerical aperture NA = 1.4. The microstructures are realized by writing successive nested shells, which is implemented via 3D Poli software (from Femtika). The first shell is the outer one that is defined by Eqs. (1-6). Inner shells are then written by reducing both R and H by a common factor, the number of steps being dependent on the aspect ratio of the structure. For instance, four shells are enough for $\alpha_0 = 5°$ in order to have fully polymerized structure in its entire volume, hence without need of additional

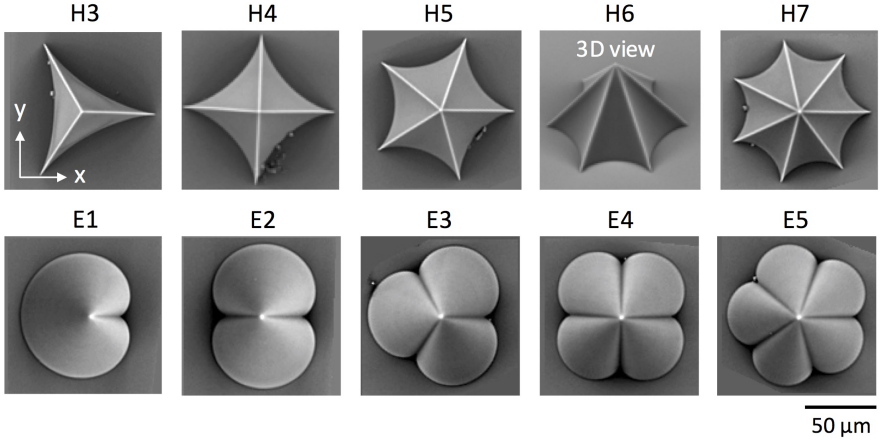

Fig. 1. Scanning electron microscope images of hypocycloidal and epicycloidal axicons of order m, Hm (m = 3 to 7) and Em (m = 1 to 5), following the designs given by Eqs. (1-6) for $R = 50$ μm and $H = 50$ μm. All the structures are imaged from top, except H6-axicon that is observed at oblique incidence in order to emphasize the three-dimensional character of the microstructures.

UV post-cure. Prior to direct laser writing, the SZ2080 material [11] is successively heated at 40, 70 and 90°C for 20 min. After exposure, the sample is immersed in 4-methyl-2-pentanone for 1 h. Obtained structures are inspected using scanning electron microscope (Hitachi TM-1000) with no additional deposition of conductive layer. A typical example is given in Fig. 1 in the case $R = H$, hence $\alpha_0 = 45°$ while further optical characterization is made for smaller values of α_0, namely $\alpha_0 = 5°$ and $15°$.

3. Optical characterization

3.1. Far-field analysis

Beam shaping capabilities of wrinkled axicons Hm ($3 \leq m \leq 6$) and Em ($1 \leq m \leq 3$) with $R = 50$ μm are experimentally assessed, first by determining their angular spectrum. This is done by placing the sample in the focal plane of a lens illuminated by a Gaussian laser beam at wavelength $\lambda = 633$ nm. Obtained beam waist radius at $\exp(-2)$ from its maximum intensity is $w_0 = 20$ μm. Then Fourier transform of the latter plane is realized by using microscope objective ($100\times$, NA $= 0.8$) whose back focal plane is imaged on a camera using a relay lens. Results are shown for $\alpha_0 = 15°$ in the second line of Fig. 2, where the first line corresponds to direct natural light imaging of the structures. In contrast to usual axicons that are characterized by ring shape Fourier spectrum, one obtains non-closed-path spectra for wrinkled axicons that are characterized by an azimuthally dependent angle $\alpha(\phi) \neq \alpha_0$ whose expression in the limit of small α_0 is

$$\alpha_{\mathrm{X}m}(\phi) = \frac{\alpha_0 R}{\left[x_{\mathrm{X}m}^2(1, \theta(\phi)) + y_{\mathrm{X}m}^2(1, \theta(\phi))\right]^{1/2}}, \tag{7}$$

with X $=$ (H, E). Experimental data is compared to simulations in the third line of Fig. 2 that shows the far-field intensity pattern I_{FF} associated with the 2D Fourier transform of the field in the plane of the sample neglecting the diffraction inside the optical element. Namely,

$$I_{\mathrm{FF}} \propto \left|\mathrm{FFT}\left[t_{\mathrm{X}m}(r, \phi) \exp(-r^2/w_0^2)\right]\right|^2, \tag{8}$$

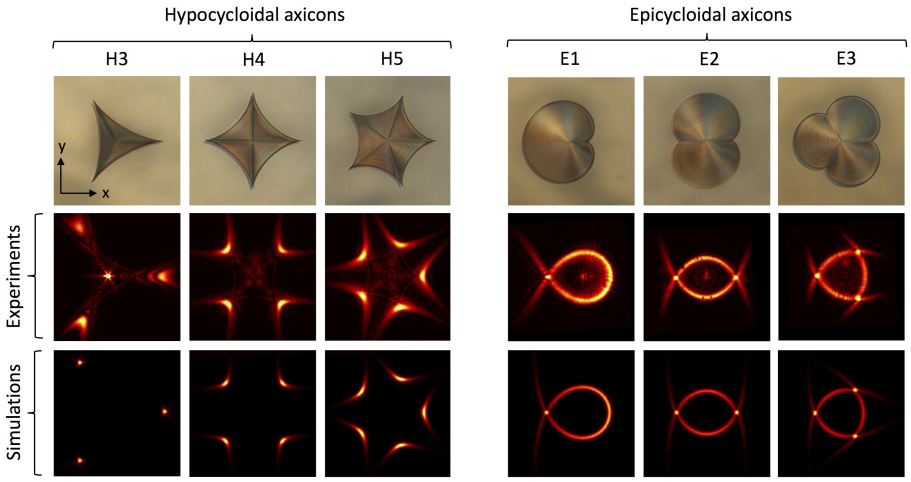

Fig. 2. Upper line: natural light imaging of a set a wrinkled axicons of hypocycloidal and epicycloidal types. Middle line: far field intensity distribution obtained by Fourier transform with a microscope objective for $R = 50$ μm and $\alpha_0 = 15°$. Bottom line: simulations from fast Fourier transform of the field just after the structure neglecting diffraction, see Eqs. (7) and (8).

where $k = 2\pi/\lambda$, $n = 1.5$, FFT refers to 2D fast Fourier transform, and

$$t_{\mathrm{X}m}(r,\phi) = \exp\left[-ikr(n-1)\alpha_{\mathrm{X}m}(\phi)\right] \tag{9}$$

is the complex amplitude transmittance mask of the wrinkled axicon Xm. Fair agreement between experimental data and calculations is obtained though we note the presence of unexpected non-zero on-axis intensity that is more pronounced for lowest-order wrinkled axicons. This can be understood noting that the incident Gaussian beam tail leaks out of the finite-size structure.

3.2. Propagation analysis: scalar treatment

The propagation behavior is retrieved by imaging the intensity distribution at distance z from the sample by translating a microscope objective (100×, NA = 0.8) along the z axis, the distance between objective and camera being kept constant. Experimental data are shown in Fig. 3 both for hypocycloidal and epicycloidal axicons, where the propagation distance is normalized to the azimuth-averaged depth of focus

$$\zeta_{\mathrm{X}m} = \frac{\zeta_0}{2\pi}\int_0^{2\pi}\frac{\alpha_0}{\alpha_{\mathrm{X}m}(\phi)}d\phi. \tag{10}$$

Observations are compared to simulations in Fig. 3 by using scalar beam propagation method based on 2D fast Fourrier transform. Namely, the intensity pattern at z, $I(x,y,z)$, is evaluated following

$$I \propto \left|\mathrm{FFT}^{-1}\left\{\exp(ik_z z)\mathrm{FFT}\left[t_{\mathrm{X}m}(r,\phi)\exp(-r^2/w_0^2)\right]\right\}\right|^2, \tag{11}$$

where FFT^{-1} refers to 2D inverse fast Fourier transform and $\exp(ik_z z)$, with $k_z = (k^2 - k_x^2 - k_y^2)^{1/2}$, is the propagation operator in the Fourier domain. Overall agreement is obtained whatever the propagation distance. Note that observed differences at $z = 0$ are merely due to the fact

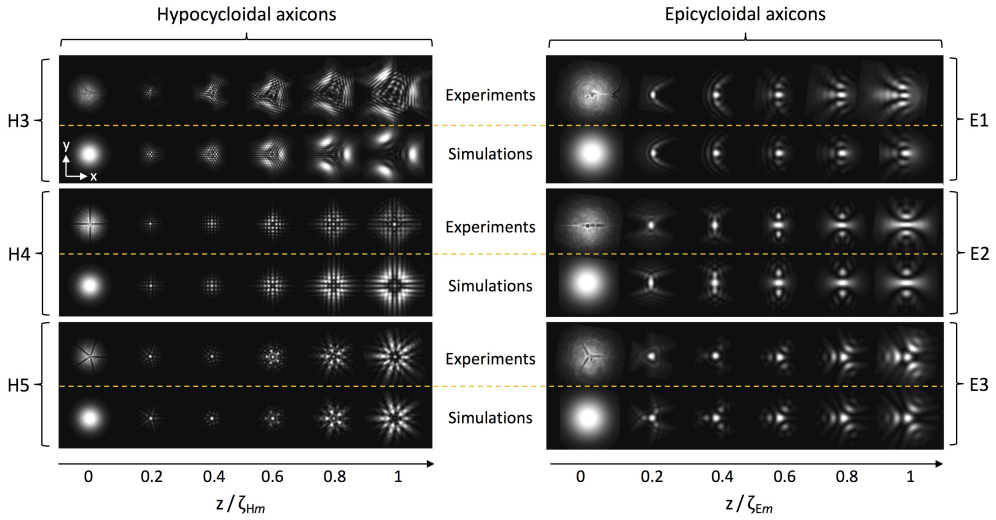

Fig. 3. Propagation analysis for a set a wrinkled axicons of hypocycloidal and epicycloidal types for $R = 50$ μm and $\alpha_0 = 5°$. For each structure, experimental intensity patterns in the (x,y) plane as a function of normalized propagation distance $z/\zeta_{\mathrm{X}m}$ are compared to beam propagation method following Eq. (11). All images are normalized to their maximal values in order to appreciate the intensity patterns despite overall intensity decrease with z.

that 3D optical elements are modeled by 2D phase masks, which prevents by construction the observation of the ridges of wrinkled axicons in the simulations.

In particular, on-axis intensity modulation may be interesting in the field of optical manipulation, in the context of so-called optical bottles [12] that refer to null intensity surrounded by bright regions in 3D. See for instance the sequence of intensity patterns at $z/\zeta_{\mathrm{H4}} = (0.4, 0.6, 0.8)$ for H4-axicon. This is explored more quantitatively by plotting the on-axis intensity distribution, as shown in Fig. 4(a) for a set of Hm-axicons with $w_0 = 20$ μm, which indicates that higher-order hypocycloidal axicons are not favorable for on-axis intensity modulation. On the other hand, the number of oscillations increases with the incident beam waist, as shown in Fig. 4(b) for $w_0 = 20$, 40 and 60 μm. Arguably, the contrast of on-axis intensity modulation is not optimal, still there are a few other better strategies to generate optical bottle arrays. One can mention the use of interferences between two Bessel beams [13], the use of Laguerre-Gaussian beams with higher-order radial index passing through usual axicon [14] or more recently the use of a birefringent axicon [15].

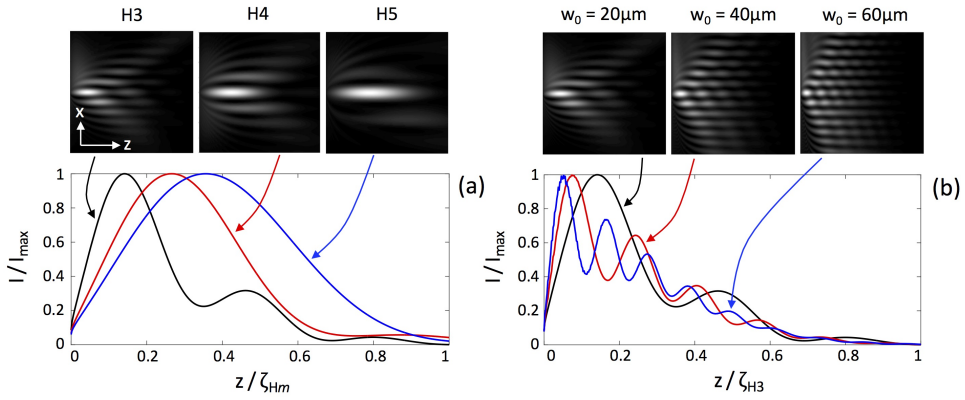

Fig. 4. (a) Calculated on-axis intensity as a function of the propagation distance for wrinkled axicons H3 (black curve), H4 (red curve) and H5 (blue curve) with $R = 50$ μm, $\alpha_0 = 5^\circ$ and $w_0 = 20$ μm. (b) Same as in panel (a) for H3-axicon and incident beam waist $w_0 = 20$, 40 and 60 μm. For both panels, upper images correspond to the corresponding intensity patterns in the plane (x, z) for -20 μm $\leq x \leq 20$ μm and $0 \leq z/\zeta_{\mathrm{H}m} \leq 1$.

3.3. *Propagation analysis: full vectorial treatment*

Although above intensity spatial modulation along the three spatial coordinates obtained within a scalar approach provides with a satisfying zero-order description of the field in the limit of small α_0 angle, the scalar approach misses beam shaping features associated with the vectorial nature of light. Indeed, it is known that focusing (i.e., nonparaxiality) is associated with spin-orbit interaction of light [16]. In the present case the focusing properties of the wrinkled axicons are azimuthally modulated as a consequence of the ϕ-dependent apex of the structures. We thus expect azimuthal features associated with the vectorial nature of light. This is investigated by performing numerical simulations of the propagation of light at the output of the structures by using a FDTD software package (FDTD Solutions, Lumerical Solutions, Inc.). The simulations do not only take into account the 3D character of the optical field, they also consider the 3D nature of the structures in contrast to scalar approach that describes the 3D structures as 2D phase masks. Practically, numerical analysis is performed for wrinkled axicons with $R = 10$, 15 and 20 μm and $\alpha_0 = 10^\circ$, 15° and 20° under plane wave illumination along the z axis. Also, we impose almost null transmission for the incident light outside the basis of the structure at $z = 0$

by placing there a perfect electrical conductor. This leads to define the azimuth-averaged depth of focus as $\zeta'_0 = R/[(n-1)\alpha_0]$ for a regular axicon and

$$\zeta'_{\mathrm{X}m} = \frac{\zeta'_0}{2\pi}\int_0^{2\pi} \frac{\alpha_0^2}{\alpha_{\mathrm{X}m}^2(\phi)}\, d\phi \tag{12}$$

for a Xm-axicon. The case of an arbitrary uniform incident polarization state is constructed by exploiting the linear superposition principle from two basic simulations performed for each structure, namely by using x-polarized and y-polarized incident light. In addition, the simulation box $x \times y \times z$ dimensions are $2R \times 2R \times \zeta'_{\mathrm{X}m}$ and perfectly matched layer is placed at its surface boundary, which prevents from unwanted effects that may arise from from finite-size calculation volume and from the way the opaque mask outside the structure basis at $z = 0$ is modeled, namely by a material with refractive index $710 + i710$.

Here we consider both left- and right-handed circular polarization states described by the unit vectors $(\mathbf{x} + \sigma i\mathbf{y})/\sqrt{2}$ with helicity $\sigma = \pm 1$. Indeed, such cases allow clear identification of nonparaxial manifestation of spin-orbit interaction of light, as illustrated in the well-known situation of a regular axicon [17] whose results are illustrated in the first line of Fig. 5 for

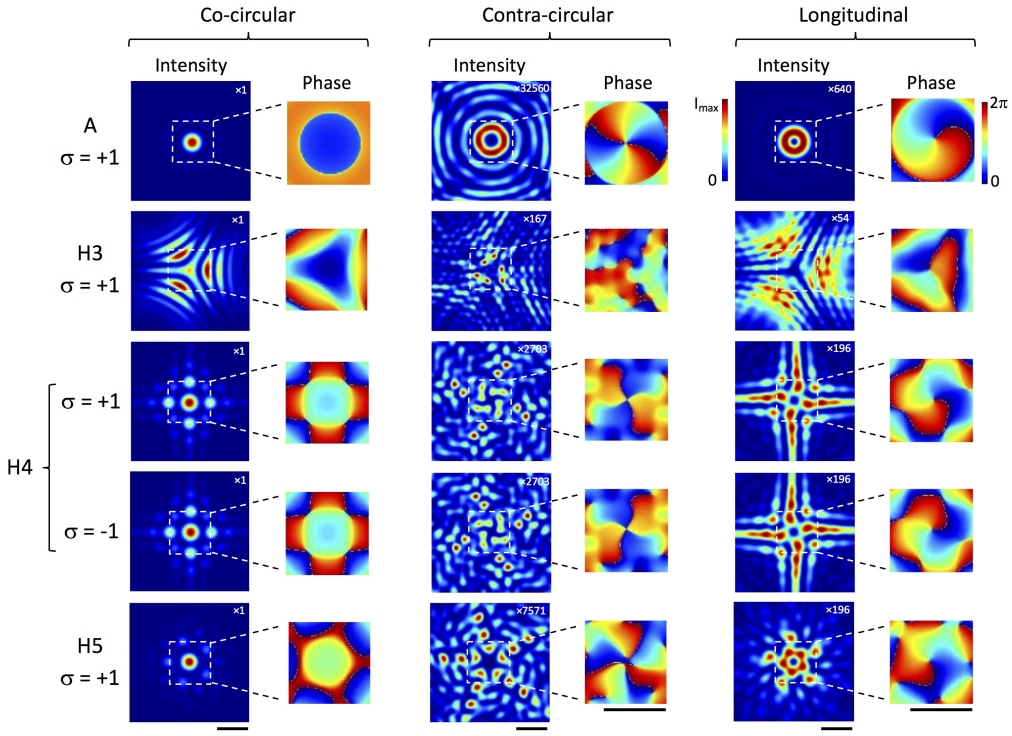

Fig. 5. FDTD simulations of the vectorial content of light in the plane located at a distance $z = \zeta'_{\mathrm{H}m}/2$ from the basis of a regular axicon (A) and hypocycloidal axicons H3, H4 and H5 in the case $R = 10$ μm and $\alpha_0 = 10°$. See text for details on simulations parameters. Incident field in a circularly polarized plane wave with helicity $\sigma = +1$, the case $\sigma = -1$ being also shown for H4 structure. Both intensity and phase of co-circularly (σ polarized), contra-circular ($-\sigma$ polarized) and longitudinal (z polarized) components of the output light field. Scale bar at the bottom of each column refers to 5 μm. The factor indicated on intensity panels refers to the ratio between the maximal intensity of the considered field component and of the co-circular component.

$\sigma = +1$, $R = 10$ μm and $\alpha_0 = 10°$. Namely, the contra-circularly polarized component of the output light field carries on-axis optical phase singularity with topological charge $\ell = 2\sigma$, as seen from the phase pattern that has an azimuthal dependence of the form $\ell\phi$. In addition, the longitudinal field component carries a phase singularity with charge $\ell = \sigma$. We note that the residual (unexpected [17]) broken axisymmetry of the intensity pattern of the contra-circular component is due to the square-shaped cross-section of the simulation box.

The situation is rather different for wrinkled axicons, as illustrated in Fig. 5 for hypocycloidal axicons Hm with $m = (3, 4, 5)$ also for $\sigma = +1$, $R = 10$ μm and $\alpha_0 = 10°$. Indeed, the circulation of the phase around the z axis nearby the z axis now depends on the order m of the axicon, namely we have $\ell = \sigma(2 - m)$. This implies a m-dependent optical spin-orbit interaction that echoes previous work on 2D form-birefringent cuspy metallic nanoslits [8, 9]. Indeed it was shown that hypocycloidal nanoslits are associated with the generation of optical phase singularities with topological charge $\ell = \sigma(2 - m)$ for the contra-circular component of the output light field, as observed here for 3D birefringence-free cuspy structures. Moreover, the helicity-dependent manifestation of the spin-orbit interaction is also checked, see Fig. 5 in the case of H4-axicon whose behavior is presented both for $\sigma = \pm 1$. Still, we note that higher-order structures eventually lead to splitting of the on-axis high-charge singularity as observed in the case of nanoslits [8, 9].

For epicycloidal geometries, the expected topological charge for the contra-circular component is $\ell = \sigma(2 + m)$ [8, 9], however on-axis higher-order topological diversity was shown not to follow such a behavior due to string translational symmetry breaking and ensuing substantial splitting of high-charge vortices. Similarly conclusions are obtained for Em-axicons. Finally, we note that our full set of simulations shows that the use of higher values of either R or α_0 also leads to high-charge splitting.

4. Conclusion

Wrinkled axicons represent a step in the conception of 3D optical elements endowed with cusps. To date, one can mention transformation-optics 3D refractive optical element enabling the measurement and sorting of orbital angular momentum of light [18, 19]. The use of cuspy designs has also been proposed previously with 2D nanoslits used to generate optical vortices from spin-orbit interaction of light owing to azimuthally varying form birefringence [8, 9]. In the context of singular optics, the particular case of hypocycloid and epicycloid curves considered here also brings spin-orbit interaction features that are associated with nonparaxiality instead of anisotropy. In addition, from the micro-optical component point of view, the fabrication of microscopic wrinkled axicons extends the set of singular optical elements fabricated by 3D direct laser writing, which was restricted so far to spiral phase plates and usual axicons [20–22].

Funding

French State managed by the French National Research Agency (ANR) in the frame of the Investments for the future Programme IdEx Bordeaux LAPHIA (ANR-10-IDEX-03-02), CONACYT Mexico, and NATO grant number SPS-985048.

Acknowledgments

Authors acknowledge the access to the swinSTAR supercomputer at Swinburne University of Technology that has been used to perform the FDTD simulations